Measurements of Impurity Transport Due to Drift-Wave Turbulence in a Toroidal Plasma

T. Nishizawa,* M. D. Nornberg, J. Boguski, D. J. Den Hartog, J. S. Sarff, Z. R. Williams, and Z. A. Xing
Department of Physics, University of Wisconsin-Madison, Madison, Wisconsin 53706, USA

D. Craig
Department of Physics, Wheaton College, Wheaton, Illinois 60187, USA

(Received 12 June 2018; revised manuscript received 11 September 2018; published 19 October 2018)

The first direct measurements of an impurity particle flux driven by drift-wave turbulence in a toroidal magnetized plasma are reported. The correlation between the impurity density and radial velocity fluctuations is measured using ion Doppler spectroscopy. The small, very fast radial velocity fluctuation is resolved with the aid of a new linearized spectrum correlation analysis method that rejects uncorrelated noise as the sample size increases. The measured C^{2+} turbulent impurity flux in the edge of the plasma is directed inward and is consistent with impurity density measurements. This is also the first direct evidence for fluctuation-induced transport due to trapped-electron-mode turbulence in reversed field pinch plasmas.

DOI: 10.1103/PhysRevLett.121.165002

Understanding and controlling impurity transport in a toroidal magnetized plasma is essential to achieve controlled fusion. The accumulation of impurity ions, i.e., those which are not fusion fuel, enhances radiation power loss and dilutes the fuel, thus threatening sustained burning plasma conditions. For toroidal confinement in a tokamak or stellarator magnetic configuration, impurity accumulation arises in part from inwardly directed neoclassical Coulomb collisional transport [1], although there is a parameter regime in which "temperature screening" helps to limit the impurity accumulation [2]. The impact of impurities tends to be exacerbated if the plasma is surrounded by high-Z metal components, as planned for the International Thermonuclear Experimental Reactor (ITER) and anticipated in future fusion reactors. Recent experiments at the Joint European Torus (JET) with an ITER-like wall illustrate the concern, and it has been necessary to identify operational scenarios that limit impurity accumulation [3]. In these scenarios, it is thought that noncollisional transport resulting from plasma turbulence helps to expel impurities [4]. Similar circumstances have been studied in other tokamak, stellarator, and reverse field pinch plasmas [5–9].

Bulk particle and heat transport in toroidal fusion plasmas are often dominated by turbulent drive mechanisms. Measurements of turbulent transport for all key plasma quantities are thus essential to develop a robust understanding of these complex plasma processes. While there have been many investigations of plasma turbulence and transport in toroidal plasmas (e.g., [10–16]) and linear devices (e.g., [17,18]), a direct measurement of fluctuation-induced impurity ion transport has not been made to our knowledge (as opposed to inferred from analysis of particle balance). Improved understanding of impurity transport will help facilitate the development of particle control strategies that could employ turbulent transport mechanisms, as in the examples noted above.

This Letter reports the first direct measurement of the turbulence-driven impurity particle flux in a high temperature toroidal plasma. Small fluctuations in the plasma flow, $\tilde{v}_r$, are resolved using a new spectral line analysis method. The line emission simultaneously yields a measurement of the fluctuating impurity particle density, $\tilde{n}_z$, so that a direct determination of the particle flux, $\Gamma_z = \langle \tilde{n}_z \tilde{v}_r \rangle$, becomes possible. The measurements are made in the edge of Madison Symmetric Torus (MST) [19] improved-confinement reversed field pinch (RFP) plasmas exhibiting density-gradient-driven trapped-electron-mode (TEM) microturbulence [20–23]. In a toroidal magnetically confined plasma, the portion of the electron population trapped within the minimum magnetic field region can facilitate an instability driven by gradients in the bulk electron density or temperature. This is also the first direct measurement of turbulent transport associated with drift-wave instability in a RFP plasma. The measured fluctuation-induced carbon flux is directed inward, which is expected for an edge-peaked impurity profile. A practical concern for the RFP is that inward impurity transport opposes favorable temperature screening of impurity ions for the RFP configuration's native classical collisional transport [24–26]. For example, this could increase the plasma's electrical resistivity, $\eta \sim Z_{\mathrm{eff}}$, and adversely affect inductive control of Magnetohydrodynamics' (MHD) tearing instabilities, apart from the basic concerns related to impurity accumulation in a fusion plasma.

Recent modeling and measurements show that drift-waves are unstable in MST plasmas when large-scale magnetic fluctuations and stochastic transport [27] are suppressed, suggesting that microturbulence could ultimately limit confinement in RFP plasmas. Tokamak-level improved-confinement conditions are achieved using inductive control of the MHD tearing instability that generates the large-scale magnetic fluctuations [28,29]. Gyrokinetic modeling based on MST experimental equilibria using the GENE code predicts that the density-gradient-driven trapped-electron mode is the fastest-growing, destabilized by the increase in plasma pressure resulting from improved confinement [20–22]. Density fluctuations measured with the far-infrared (FIR) laser interferometer in 200 kA plasmas exhibit a critical-density-gradient threshold, $R_0/L_n = R_0|\nabla n_e|/n_e \gtrsim 18$, consistent with the GENE modeling [23]. The measured fluctuations are localized to the strong density gradient region, $r/a \approx 0.8$, and the spectrum peaks at $k_\perp \rho_s \sim 0.15$, where $k_\perp$ is the perpendicular wave number and $\rho_s \approx 1.5$ cm is the ion sound gyroradius. The modeling and measurements reveal the importance of residual large-scale magnetic fluctuations that disrupt zonal flow and allow the TEM turbulence to saturate at a density gradient near the linear stability threshold [22]. While the interferometer density measurements are consistent with the GENE modeling, they do not address the predicted energy and particle transport associated with the TEM turbulence.

The measurements reported here were made in improved-confinement MST plasmas with a plasma current, $I_p = 380$ kA, line-averaged density, $\bar{n}_e = 0.6 \times 10^{19}$ m^{-3}, and central electron temperature, $T_e(r = 0) = 1$ keV. The major and minor radii of the plasma are $R_0 = 1.5$ m and $a = 0.5$ m respectively. A high-throughput, narrow-bandpass spectrometer sensitive to emissions in the near-UV to blue [30,31] is used to measure the impurity line emission from C^{2+} ions located in the outer region of the plasma. Carbon is an intrinsic impurity in MST plasmas sublimated from graphite limiters mounted on the interior vessel wall. The light emission from this low charge state of carbon is stimulated by collisions with thermal electrons.

The C^{2+} emission yields new information about the TEM microturbulence and provides the basis for direct measurements of the fluctuation-induced impurity particle flux. The viewing geometry is shown in Fig. 1. The duo spectrometer collects light via optical fibers that view the plasma radially through a porthole in the MST's close-fitting aluminum shell, shown in grey. The observed Doppler shift is therefore due to the radial velocity of the plasma flow. The C^{2+} 464.7 nm emission shell, shown in light blue, is calculated using the charge-state profiles obtained from a previous analysis using a time-dependent one-dimensional collisional-radiative impurity transport code [26]. The location and extent of the predicted emission profile are consistent with radiance measurements taken across the poloidal cross section. The pink and green light

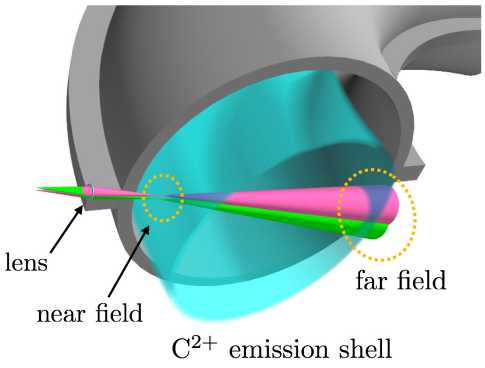

FIG. 1. The viewing geometry for the C^{2+} transport measurements. A duo spectrometer [30] accepts two spatial channels whose optical ray paths, shown in pink and green, can be adjusted in relative orientation. For the transport measurement, the two views are radial within 5°, and the near-field foci separation is aligned to the pitch of the magnetic field.

cones are focused on the near field where the rays pass through the C^{2+} shell the first time. The relative separation of the light cones at the focal point is 1.6 cm, which is comparable to ρ_s. The rays pass through the C^{2+} shell again in the far field, and therefore, each spatial channel collects C^{2+} emission light from the near and far fields. We treat the contribution from the far field as a dc component since small-spatial-scale fluctuations are averaged out in the far field's larger sample volume.

Example waveforms for a typical improved-confinement plasma that exhibits the emergence of TEM microturbulence are shown in Fig. 2, which includes data from the (a) high-throughput spectrometer, (b) high-bandwidth FIR

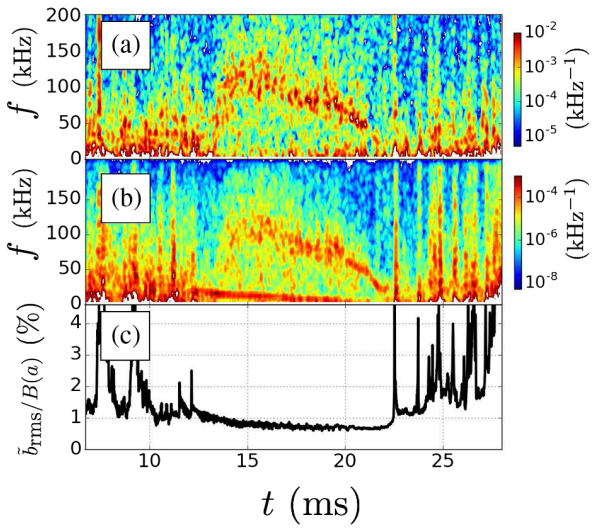

FIG. 2. (a) Spectrogram of normalized C^{2+} 464.7 nm emission intensity fluctuations. (b) Spectrogram of normalized chord-integrated electron density intensity fluctuations at impact parameter $R - R_0 = 43$ cm ($r/a = 0.86$). (c) Tangential component of normalized magnetic fluctuations at $r = a$.

interferometer [32,33], and (c) magnetic fluctuations measured by a toroidal array of pickup loop sensors at $r = a$. Before 10 ms, tearing instabilities (<50 kHz) cause large fluctuations in the C^{2+} emission and electron density, illustrated by the spectrograms in Figs. 2(a) and 2(b). The electron density fluctuations associated with the tearing instability have been studied previously in the MST [34,35]. The improved confinement period begins at 10 ms, and the amplitude of magnetic fluctuations is greatly reduced, indicated by the reduction in $\tilde{b}_{\mathrm{rms}}/B(a)$ shown in Fig. 2(c). The electron density gradient steepens at $r/a \gtrsim 0.7$, and high-frequency (~100 kHz) fluctuations emerge in both the C^{2+} line emission and electron density.

Two fiber optic views are employed with toroidal separation to measure the perpendicular wavelength using two-point correlation methods (N. B., the poloidal field is dominant in the edge region of an RFP). An ensemble of C^{2+} line emission data from similar discharges was obtained to analyze the frequency-wavelength power spectrum. While not shown here, the spectral power density peaks at $k_\perp \rho_i \sim 0.25$ and spreads to $k_\perp \rho_i \sim 0.7$, where $k_\perp \approx k_\phi$. The peak is at modestly higher $k_\perp$ than in 200 kA plasmas [23]. The mode propagation is in the electron diamagnetic drift direction in the plasma rest frame, as expected for an electron-branch drift wave. With the views oriented instead along the magnetic field, we find $k_{||} \ll k_\perp$. (The small field-aligned separation of the fiber optic focii makes it difficult to precisely measure $k_{||}$.) These observations are consistent with expectations for the density-gradient-driven TEM predicted by GENE modeling. Also, the power spectrum (Fig. 2) is relatively narrow, which is similar to the "quasicoherent" characteristic of TEM turbulence observed in tokamak plasmas [36–38].

A direct measurement of the fluctuation-induced impurity particle flux is possible because the spectral emission of C^{2+} yields information on $\tilde{v}_r$ due to the Doppler shift of the line emission and $\tilde{n}_z$ through the emission strength. While $\tilde{v}_r$ is measured directly through the Doppler shift (if resolved), obtaining the C^{2+} density fluctuation, $\tilde{n}_{C^{2+}}$, is less straightforward. Under the relevant plasma conditions, electron impact excitation is the dominant process through which C^{2+} ions radiate at 464.7 nm (recombination and charge exchange are negligible). The ion charge-state balance can be considered quasistatic since it evolves on the longer collisional time scale. The emission coefficient for electron-impact collisions is

$$\varepsilon = n_e n_{C^{2+}} \mathrm{PEC}(T_e), \tag{1}$$

where n_e is the electron density, $n_{C^{2+}}$ is the C^{2+} ion density, and PEC is a photon emission coefficient for the $\lambda_0 =$ 464.7 nm C^{2+} emission line that contains the collisional excitation cross section and branching fraction for the transition. As a drift wave passes through the line of sight, there is a radial plasma displacement of order ρ_s that

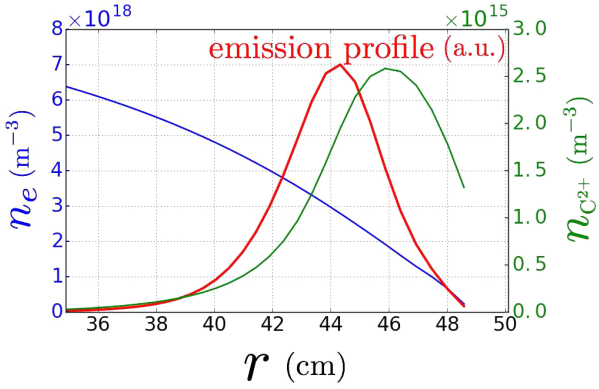

FIG. 3. Profiles for n_e, $n_{C^{2+}}$, and C^{2+} 464.7 nm emission. Note that, the emission is strongest where the electron and C^{2+} density gradients are in opposite directions.

advects plasma along the gradient direction of these quantities, which results in a fluctuation in each quantity in Eq. (1). From the continuity equation, the relative fluctuation amplitude in the particle densities due to this advective motion is related to the inverse gradient scale length, e.g., $i\omega\tilde{n}_e = \tilde{\mathbf{v}} \cdot \boldsymbol{\nabla} n_e$. Similar relations hold for the impurity density and temperature. By linearizing and normalizing Eq. (1), we have

$$\frac{\tilde{\varepsilon}}{\varepsilon_0} = \frac{\tilde{n}_{C^{2+}}}{n_{C^{2+},0}} + \frac{\tilde{n}_e}{n_{e,0}} + \alpha \frac{\tilde{T}_e}{T_{e,0}} \tag{2}$$

$$= \frac{i\tilde{v}_r}{\omega}\left(L^{-1}_{n_{C^{2+}}} - L^{-1}_{n_e} - \alpha L^{-1}_{T_e}\right), \tag{3}$$

where

$$\alpha \equiv \frac{T_{e,0}}{\mathrm{PEC}(T_{e,0})} \frac{d\mathrm{PEC}}{dT_e}(T_{e,0}) \tag{4}$$

and $L_{T_e} = T_{e,0}/|\nabla T_{e,0}|$, $L_{n_e} = n_{e,0}/|\nabla n_{e,0}|$, and $L_{n_{C^{2+}}} = n_{C^{2+},0}/|\nabla n_{C^{2+},0}|$. Profiles of $n_{e,0}$, $n_{C^{2+},0}$, and ε_0 for the C^{2+} 464.7 nm line emission [39] are shown in Fig. 3. The line-averaged α is about 0.34 under the assumption that $\tilde{T}_e/T_{e,0}$ is constant over the emission shell. At the peak of the emission shell, $L_{C^{2+}} \sim 1.5$ cm while L_{n_e}, $L_{T_e} \sim 6.0$ cm suggesting that the dominant source of the emission fluctuations is due to advection of the impurity so that $\tilde{\varepsilon}/\varepsilon \approx \tilde{n}_{C^{2+}}/n_{C^{2+},0}$. Note as well that the outward-directed C^{+2} density gradient implies $\tilde{n}_{C^{2+}}$ has opposite phase relative to $\tilde{n}_e$ and $\tilde{T}_e$.

Even with the use of a high-étendue spectrometer with amplification from photomultiplier tubes, we do not collect sufficient photons on the drift-wave fluctuation time scale ($2\pi/\omega \sim 10$ μs) using conventional emission line fitting techniques. Instead, we use linearized spectrum correlation analysis (LSCA) [40]. In LSCA, we subdivide spectral channels into two groups, A and B [as in Figs. 4(a) or 4(b)],

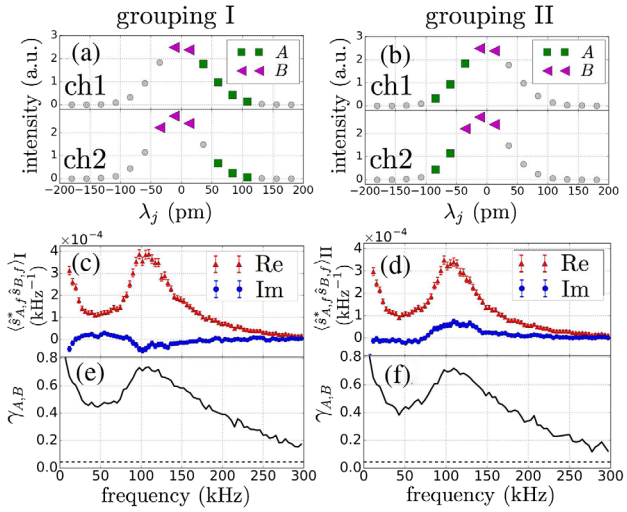

FIG. 4. (a) and (b): spectral channel groupings. (c) and (d): cross spectra. (e) and (f): coherence. The dashed lines in (e) and (f) are a statistical significance level. λ_j is the wavelength of spectral channel j with respect to 464.7 nm.

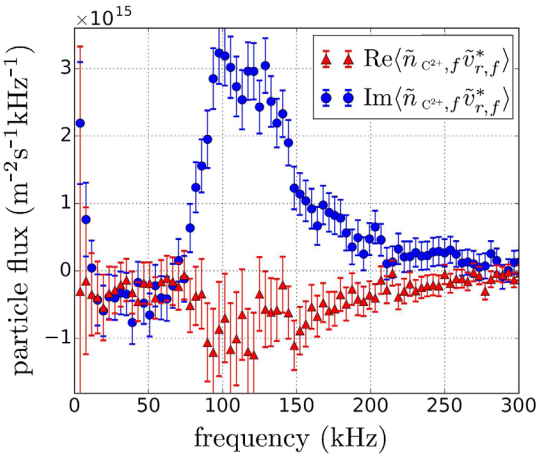

FIG. 5. Spectral density of the impurity particle flux (red triangles) and the circulating flow (blue circles) due to drift wave turbulence.

and we sum the signals in each group to create two time series. The two fiber optic views are aligned to match the pitch of the magnetic field to provide independent measurements within a correlation length (recall $k_\parallel \ll k_\perp$). We define $\hat{s}_{A,f}$ and $\hat{s}_{B,f}$ to be the complex Fourier transformation of group A and B at frequency f. The distribution function for the impurity ions is assumed to remain close to a Maxwell-Boltzmann distribution so that fluctuations in the spectral emission coefficient should have a Gaussian line shape defined by the total emission fluctuations (which scale with the ion density fluctuations $\tilde{n}_{C^{2+},f}/n_{C^{2+},0}$, ion velocity fluctuations $\tilde{v}_{r,f}$, and C^{2+} temperature fluctuations $\tilde{T}_{C^{2+},f}$). Linearizing the fluctuations in the line shape allows us to write

$$\hat{s}_{A,f} \approx \frac{\tilde{n}_{C^{2+}}}{n_{C^{2+},0}} + \frac{k_A \lambda_0}{c}\tilde{v}_{r,f} + \frac{c_{T,A}\lambda_0^2}{m_C c^2}\tilde{T}_{C^{2+},f} + x_{A,f}, \quad (5)$$

where the coefficients k_A and $c_{T,A}$ depend on the steady state emission line shape measured in spectral channels in group A, and $x_{A,f}$ is the contribution from uncorrelated fluctuations. We use c and m_C for the speed of light and the mass of carbon. The expression for $\hat{s}_{B,f}$ is similar. When groups A and B are composed of distinct channels, the cross spectrum $\langle\hat{s}^*_{A,f}\hat{s}_{B,f}\rangle$ reflects fluctuations in the emission line shape while rejecting noise, $x_{A,f}$ and $x_{B,f}$. The physical quantities of interest can be extracted by making different groupings for A and B and iterating the same steps.

We analyze two sets of channels, groupings I and II shown in Figs. 4(a) and 4(b), such that

$$\mathrm{Re}\langle\hat{s}^*_{A,f}\hat{s}_{B,f}\rangle_\mathrm{I} - \mathrm{Re}\langle\hat{s}^*_{A,f}\hat{s}_{B,f}\rangle_\mathrm{II} \approx \mathrm{Re}\langle\tilde{n}_{C^{2+},f}\tilde{v}^*_{r,f}\rangle\frac{\lambda_0}{n_{C^{2+},0}c}(\langle k_A + k_B\rangle_\mathrm{I} - \langle k_A + k_B\rangle_\mathrm{II}) \quad (6)$$

where $\tilde{\varepsilon}/\varepsilon \approx \tilde{n}_{C^{2+}}/n_{C^{2+},0}$ is assumed. The triangle brackets with a subscript represent the ensemble average of a channel grouping specified by the subscript; e.g., $\langle X\rangle_\mathrm{I}$ is the ensemble average of a certain quantity, X for grouping I. The cross-spectra and coherence levels for each grouping are shown in Figs. 4(c)–4(f). Since $\langle k_A + k_B\rangle_\mathrm{I}$ and $\langle k_A + k_B\rangle_\mathrm{II}$ can be calculated from the time-averaged emission line shape and the spectral transfer functions of the spectrometer, we can infer the particle transport $\mathrm{Re}\langle\tilde{n}_{C^{2+},f}\tilde{v}^*_{r,f}\rangle$ from Eq. (6).

The spectral density of the measured impurity particle flux $\Gamma_{C^{2+}} = \mathrm{Re}\langle\tilde{n}_{C^{2+},f}\tilde{v}^*_{r,f}\rangle$ is shown in Fig. 5, which reveals net inward transport of C^{2+} in the frequency range 80–250 kHz that corresponds to TEM turbulence. The $\mathrm{Im}\langle\tilde{n}_{C^{2+},f}\tilde{v}^*_{r,f}\rangle$ component is determined from an equation similar to Eq. (6) [40], and its positive value (Fig. 5) is consistent with a $\pi/2$ relative phase expected from Eq. (3) when the emission fluctuations are dominated by impurity density for waves propagating in the electron diamagnetic direction. Integrating over the frequency range associated with the TEM turbulence (80 to 250 kHz), the inward C^{2+} flux is $\Gamma_{C^{2+},\mathrm{turb}} = 8.6 \pm 0.9 \times 10^{16}\ \mathrm{m^{-2}\,s^{-1}}$. The neglected contributions from $\tilde{n}_e$ and $\tilde{T}_e$ have the opposite phase as $\tilde{n}_{C^{2+}}$. Thus the flux may be underestimated. The rms amplitude of $\tilde{n}_{C^{2+}}$ is straightforwardly measured using a group of wavelength channels that symmetrically span the peak at $\lambda_j \approx 0$, which yields $|\tilde{n}_{C^{2+}}|/n_{C^{2+},0} = 0.16 \pm 0.01$. Similarly, the rms amplitude of $\tilde{v}_r$ is measured using groups of channels taken equally from either side of the peak to maximize sensitivity to the blue and red shift, which yields $|\tilde{v}_r| = 0.8 \pm 0.2$ km/s.

Previous impurity particle balance analysis for MST plasmas yielded estimates for the fully-stripped C^{6+} diffusion coefficient, D_ex, and the (outward) convection velocity, v_ex [26]. The coefficients for classical collisional transport, D_cl and v_cl, were also evaluated. For 380 kA pulsed

poloidal current drive (PPCD) plasmas, $D_{ex} \approx 1.5\ m^2/s$, $D_{cl} \approx 0.5\ m^2/s$, $v_{ex} \approx -15\ m/s$, and $v_{cl} \approx -20\ m/s$ at $r/a = 0.9$. A comparison of the C^{6+} particle balance with the directly-measured turbulent particle flux for C^{2+} exposes the importance of turbulent transport in these plasmas. If $\Gamma_{C^{2+},turb}$ is convection dominated, then $\Gamma_{C^{2+},turb}/n_{C^{2+},0} \simeq -48 \pm 5\ m/s$. If $\Gamma_{C^{2+},turb}$ is diffusive, then $\Gamma_{C^{2+},turb}/\nabla n_{C^{2+},0} \simeq 0.72\ m^2/s$. These values are significant compared with either D_{ex} and v_{ex}, or D_{cl} and v_{cl}. This implies that turbulence plays an important role in impurity particle balance. It is also the first direct experimental evidence for significant transport associated with TEM turbulence in improved-confinement RFP plasmas.

The TEM fluctuations are expected to be dominantly electrostatic, and therefore all species have the same flow fluctuation, $\tilde{\mathbf{v}} \approx \tilde{\mathbf{E}} \times \mathbf{B}_0$. While the emission fluctuations are dominated by C^{2+} impurities, the LSCA measurement of $|\tilde{v}_r| \simeq 0.8\ km/s$ allows an upper-bound estimate of the electron flux associated with the TEM turbulence using an independent measurement of $\tilde{n}_e$ obtained from FIR interferometry (as in [23]). For the plasmas described here, $|\tilde{n}_e| \simeq 1.4 \times 10^{17}\ m^{-3}$ for the 80–250 kHz frequency range at $r/a = 0.8$. Therefore, $\Gamma_{e,turb} = \langle \tilde{n}_e \tilde{v}_r \rangle \leq |\tilde{n}_e||\tilde{v}_r| \simeq 1.1 \times 10^{20}\ m^{-2}\ s^{-1}$. Unfortunately the port access on the MST does not easily permit the spectroscopic measurement to be located within a TEM correlation length of the FIR interferometer, so the cross-correlation phase is not known. Previous global particle balance analysis yielded $\Gamma_{e,ex} \simeq 2 \times 10^{20}\ m^{-2}\ s^{-1}$ in the edge of similar PPCD plasmas [34]. Therefore, TEM turbulence is likely to be a significant contributor to electron transport in the edge. A complete measurement of the electron flux is warranted via diagnostic upgrades or insertable probes to determine whether microturbulence is the dominant electron transport mechanism.

In summary, we have, for the first time, directly measured the transport of impurity ions associated with microturbulence in a toroidal magnetically confined plasma. The Doppler shift and impurity density fluctuations are resolved using a high-performance spectrometer and a new spectral analysis method. This is the first evidence for transport associated TEM microturbulence in improved-confinement RFP plasmas, helping to confirm predictions from gyrokinetic modeling. The measurement techniques used here can be applied to other high temperature plasmas to measure velocity fluctuations and characterize the turbulent transport of impurities and electrons.

The authors would like to thank Dr. T. Barbui for providing measurements of the carbon impurity profiles, Dr. P. W. Terry and Dr. M. J. Pueschel for valuable discussions, and Dr. J. R. Duff and Dr. E. Parke for the FIR measurements. This work is supported by the U.S. Department of Energy, Office of Science, and Office of Fusion Energy Sciences under Award No. DE-FC02-05ER54814.

*Current address: Max-Planck-Institut für Plasmaphysik, Greifswald, Germany.
takashi.nishizawa@ipp.mpg.de

[1] S. Hirshman and D. Sigmar, Nucl. Fusion **21**, 1079 (1981).
[2] M. R. Wade, W. A. Houlberg, and L. R. Baylor, Phys. Rev. Lett. **84**, 282 (2000).
[3] M. E. Puiatti, M. Valisa, C. Angioni, L. Garzotti, P. Mantica, M. Mattioli, L. Carraro, I. Coffey, and C. Sozzi (JET-EFDA Contributors), Phys. Plasmas **13**, 042501 (2006).
[4] C. Angioni and A. G. Peeters, Phys. Rev. Lett. **96**, 095003 (2006).
[5] M. Yoshinuma, K. Ida, M. Yokoyama, M. Osakabe, K. Nagaoka, S. Morita, M. Goto, N. Tamura, C. Suzuki, S. Yoshimura, H. Funaba, Y. Takeiri, K. Ikeda, K. Tsumori, and O. Kaneko (the LHD Experimental Group), Nucl. Fusion **49**, 062002 (2009).
[6] S. Sudo, Plasma Phys. Controlled Fusion **58**, 043001 (2016).
[7] E. Scavino, J. S. Bakos, R. Dux, and H. Weisen (TCV Team), Plasma Phys. Controlled Fusion **45**, 1961 (2003).
[8] C. Angioni, R. Bilato, F. Casson, E. Fable, P. Mantica, T. Odstrcil, and M. Valisa (ASDEX Upgrade Team and JET Contributors), Nucl. Fusion **57**, 022009 (2017).
[9] I. Predebon, L. Carraro, and C. Angioni, Plasma Phys. Controlled Fusion **53**, 125009 (2011).
[10] W. Horton, Rev. Mod. Phys. **71**, 735 (1999).
[11] P. C. Liewer, Nucl. Fusion **25**, 543 (1985).
[12] C. Bourdelle, Plasma Phys. Controlled Fusion **47**, A317 (2005).
[13] S. Menmuir, L. Carraro, A. Alfier, F. Bonomo, A. Fassina, G. Spizzo, and N. Vianello, Plasma Phys. Controlled Fusion **52**, 095001 (2010).
[14] N. Howard, M. Greenwald, D. Mikkelsen, M. Reinke, A. White, D. Ernst, Y. Podpaly, and J. Candy, Nucl. Fusion **52**, 063002 (2012).
[15] P. Terry, D. Carmody, H. Doerk, W. Guttenfelder, D. Hatch, C. Hegna, A. Ishizawa, F. Jenko, W. Nevins, I. Predebon, M. Pueschel, J. Sarff, and G. Whelan, Nucl. Fusion **55**, 104011 (2015).
[16] S. Liu, S. Guo, W. Kong, and J. Dong, Nucl. Fusion **54**, 043006 (2014).
[17] M. J. Burin, G. R. Tynan, G. Y. Antar, N. A. Crocker, and C. Holland, Phys. Plasmas **12**, 052320 (2005).
[18] S. Chakraborty Thakur, R. Hong, and G. R. Tynan, Rev. Sci. Instrum. **89**, 10J117 (2018).
[19] R. Dexter, D. Kerst, T. Lovell, S. Prager, and J. Sprott, Fusion Sci. Technol. **19**, 131 (1991).
[20] D. Carmody, M. J. Pueschel, and P. W. Terry, Phys. Plasmas **20**, 052110 (2013).
[21] D. Carmody, M. J. Pueschel, J. K. Anderson, and P. W. Terry, Phys. Plasmas **22**, 012504 (2015).
[22] Z. R. Williams, M. J. Pueschel, P. W. Terry, and T. Hauff, Phys. Plasmas **24**, 122309 (2017).
[23] J. R. Duff, Z. R. Williams, D. L. Brower, B. E. Chapman, W. X. Ding, M. J. Pueschel, J. S. Sarff, and P. W. Terry, Phys. Plasmas **25**, 010701 (2018).
[24] S. T. A. Kumar, D. J. Den Hartog, K. J. Caspary, R. M. Magee, V. V. Mirnov, B. E. Chapman, D. Craig, G. Fiksel, and J. S. Sarff, Phys. Rev. Lett. **108**, 125006 (2012).
[25] S. T. A. Kumar, D. J. Den Hartog, V. V. Mirnov, K. J. Caspary, R. M. Magee, D. L. Brower, B. E. Chapman,

D. Craig, W. X. Ding, S. Eilerman, G. Fiksel, L. Lin, M. Nornberg, E. Parke, J. A. Reusch, and J. S. Sarff, Phys. Plasmas **19**, 056121 (2012).
[26] T. Barbui, L. Carraro, D. J. Den Hartog, S. T. A. Kumar, and M. Nornberg, Plasma Phys. Controlled Fusion **56**, 075012 (2014).
[27] J. A. Reusch, J. K. Anderson, D. J. Den Hartog, F. Ebrahimi, D. D. Schnack, H. D. Stephens, and C. B. Forest, Phys. Rev. Lett. **107**, 155002 (2011).
[28] J. Sarff *et al.*, Nucl. Fusion **43**, 1684 (2003).
[29] B. E. Chapman *et al.*, Plasma Phys. Controlled Fusion **52**, 124048 (2010).
[30] D. Craig, D. J. Den Hartog, D. A. Ennis, S. Gangadhara, and D. Holly, Rev. Sci. Instrum. **78**, 013103 (2007).
[31] T. Nishizawa, M. D. Nornberg, D. J. Den Hartog, and D. Craig, Rev. Sci. Instrum. **87**, 11E530 (2016).
[32] D. L. Brower, W. X. Ding, S. D. Terry, J. K. Anderson, T. M. Biewer, B. E. Chapman, D. Craig, C. B. Forest, S. C. Prager, and J. S. Sarff, Rev. Sci. Instrum. **74**, 1534 (2003).
[33] W. X. Ding, L. Lin, J. R. Duff, D. L. Brower, and J. S. Sarff, Rev. Sci. Instrum. **83**, 10E302 (2012).
[34] N. E. Lanier, D. Craig, J. K. Anderson, T. M. Biewer, B. E. Chapman, D. J. Den Hartog, C. B. Forest, S. C. Prager, D. L. Brower, and Y. Jiang, Phys. Plasmas **8**, 3402 (2001).
[35] L. Lin, W. X. Ding, D. L. Brower, W. F. Bergerson, T. A. Carter, T. F. Yates, A. F. Almagri, B. E. Chapman, and J. S. Sarff, Phys. Rev. Lett. **108**, 175001 (2012).
[36] H. Arnichand, R. Sabot, S. Hacquin, A. Krämer-Flecken, X. Garbet, J. Citrin, C. Bourdelle, G. Hornung, J. Bernardo, C. Bottereau, F. Clairet, G. Falchetto, and J. Giacalone, Nucl. Fusion **54**, 123017 (2014).
[37] J. C. Hillesheim, J. C. DeBoo, W. A. Peebles, T. A. Carter, G. Wang, T. L. Rhodes, L. Schmitz, G. R. McKee, Z. Yan, G. M. Staebler, K. H. Burrell, E. J. Doyle, C. Holland, C. C. Petty, S. P. Smith, A. E. White, and L. Zeng, Phys. Rev. Lett. **110**, 045003 (2013).
[38] W. L. Zhong, X. L. Zou, C. Bourdelle, S. D. Song, J. F. Artaud, T. Aniel, and X. R. Duan, Phys. Rev. Lett. **111**, 265001 (2013).
[39] The emission profile is calculated using a PEC generated with ADAS.
[40] T. Nishizawa, M. D. Nornberg, D. J. Den Hartog, and J. S. Sarff, Rev. Sci. Instrum. **88**, 083513 (2017).